Self-archived version of the article published in Chemical Engineering Science:
N. Cancilla, M. Ciofalo, A. Cipollina, A. Tamburini, G. Micale
Straight fiber bundles with non-uniform porosity: shell-side hydrodynamics and mass transfer in cross flow, Chemical Engineering Science, 291, 2024, 119947.
https://doi.org/10.1016/j.ces.2024.119947

Straight fiber bundles with non-uniform porosity: shell-side hydrodynamics and mass transfer in cross flow

N. Cancilla, M. Ciofalo, A. Cipollina, A. Tamburini*, G. Micale

Dipartimento di Ingegneria, Università degli Studi di Palermo
Viale delle Scienze Ed. 6, 90128 Palermo, Italy

*corresponding author: alessandro.tamburini@unipa.it

Abstract

This study explores fully developed shell-side hydrodynamics and mass transfer past straight fiber bundles with non-uniform porosity in cross-flow. Simplified geometries made up by a checkerboard array of alternately high porosity and low porosity regions are considered. Simulations are performed for two domain sizes: a small geometry (26 fibers) and a large geometry (104 fibers). In the small geometry, the Darcy friction coefficient (f_T) exhibits hydraulic isotropy at low transverse flow Reynolds numbers (Re_T) but becomes dependent on the flow attack angle (θ) at higher Re_T. In the large geometry, this dependency is observed at lower Re_T. Non-uniform porosity, reduces f_T at almost all Re_T and θ in the small geometry, with the large geometry exhibiting a more complex behavior. Regarding mass transfer, up to $\mathrm{Re}_T\approx$1-10 (depending on θ), a non-uniform porosity leads to lower Sherwood numbers compared to regular square arrays. However, at higher Re_T, it enhances mass transfer.

Keywords: Hollow fiber; non-uniform porosity; friction coefficient; Sherwood number; Computational Fluid Dynamics; cross flow.

1. Introduction

The extensive adoption of hollow fiber membrane contactors across numerous applications, particularly in the field of separation processes technology, has kindled a growing interest in the detailed investigation of these devices to enhance their performance. These applications encompass a range of processes, including membrane distillation (Yang et al., 2012), gas separation (Ibrahim et al., 2018), filtration (Nakatsuka et al., 1996), reverse osmosis (Bansal and Gill, 1982), blood oxygenation (Teber et al., 2022) and hemodialysis (Cancilla et al., 2022). In hollow-fiber contactors, the interaction between two fluids occurs through the pores of a semipermeable membrane. The fibers themselves possess a cylindrical shape and are organized in bundles within a contactor or module, facilitating the separation of these two phases. The number of fibers within the module and the inner diameter of the shell housing are the key factors determining the packing density.

Figure 1 offers a cross-sectional view of a hollow fiber module designed for hemodialysis applications. This image, obtained through a standard scanner, was created by injecting a two-component resin into the shell side, allowing it to cure, and subsequently slicing a thin section for examination.

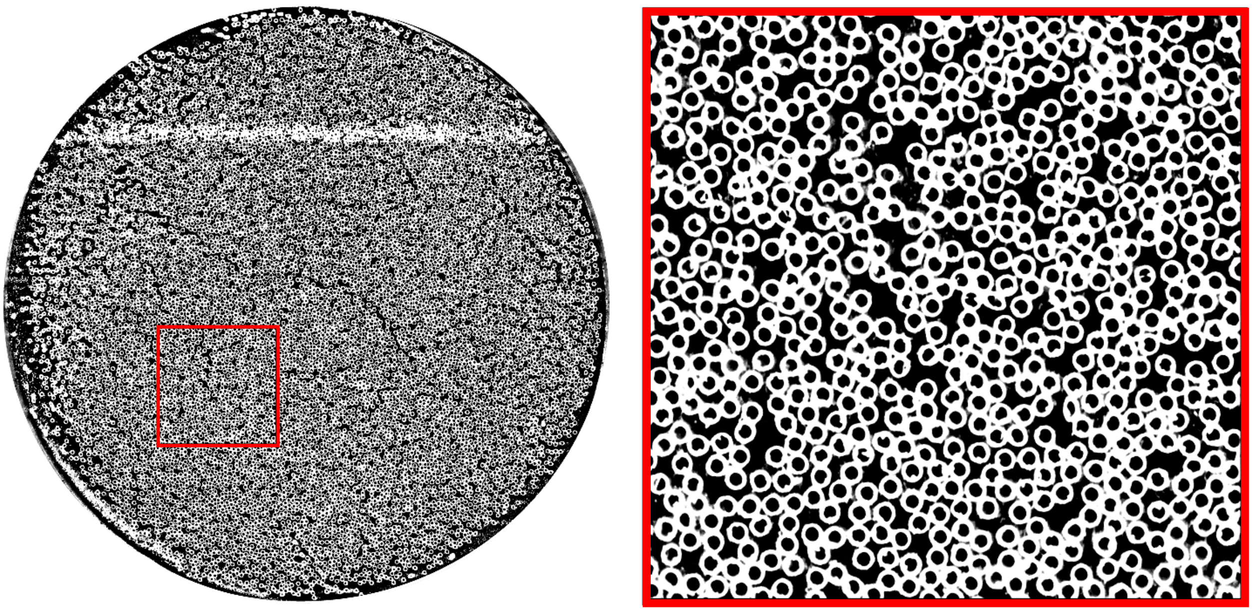

(a) (b)

Figure 1: Cross section of a hollow-fiber bundle for hemodialysis applications, showing the random arrangement of the fibers. (a): whole bundle (~10,000 fibers, diameter ~40 mm, porosity ~0.5); the light horizontal band is an artifact resulting from the cutting process. (b): 8×8 mm square detail. The outer diameter of each fiber is ~280 μm.

In **Figure 1**(a), a substantial irregularity is evident within the large-scale arrangement of the fiber bundle. Notably, the peripheral region near the cylindrical housing displays a significantly lower packing density compared to the central region. Even within the central area, as illustrated in **Figure 1**(b), where the packing density seems to exhibit a more statistically uniform pattern, one can observe scattered gaps intermingled with clusters of densely packed fibers. This sporadic distribution is an inherent outcome of the randomic nature of the arrangement. Similar insights were also presented by Frank *et al.* (Frank et al., 2000). In their experimental studies involving a commercial hemodialysis module, they employed a much more sophisticated 3-D technique, the computational tomography. Their findings disclosed the presence of substantial variations in fiber packing: the most tightly packed fibers were concentrated in the core of the fiber bundle, while the regions with the lowest fiber density were situated along the perimeter.

As early as 1979, Noda *et al.* (Noda et al., 1979) identified and characterized fluid maldistribution within the modules using tracer analysis. They correlated this issue with the presence of less densely packed fiber bundle regions. Moreover, they successfully simulated this behavior using a simple model based on the concept of a bypass.

However, the prevailing method found in the literature for modeling a hollow fiber contactor involves the assumption that the fibers are organized in a structured lattice, often taking the form of squares or triangles, akin to the design seen in traditional shell-and-tube heat exchangers. Numerous researchers (Cancilla et al., 2021; Dierickx et al., 2001; Dwyer and Berry, 1970; Happel, 1959; Ishimi et al., 1987; Miyagi, 1958; Miyatake and Iwashita, 1991, 1990; Noda and Gryte, 1979; Sparrow and Loeffler, 1959) have extensively delved into topics concerning fluid dynamics and, in certain instances, mass transfer, focusing on fiber bundles assumed to be tightly packed in regular lattices.

In a recent study, Sun *et al.* (Sun et al., 2022) explored by CFD the repercussions of deviating from an initially uniform distribution of fibers. They investigated how radial irregularities in porosity between the core region and the interface where fibers meet the housing impact the overall performance of a gas separation module in fully developed axial flow, finding a significant reduction in module performance.

Other investigations explored entirely random arrangements (Bao et al., 1999; Bao and Lipscomb, 2002a, 2002b; Chen and Hlavacek, 1994; Rogers and Long, 1997). Among these, Bao and Lipscomb employed Voronoi tessellation (Voronoi, 1908) to enclose each fiber with a polygonal contour in random distributions. Their comprehensive study meticulously examined both fully developed conditions (Bao and Lipscomb, 2002a, 2002b) and the entry region (Bao et al., 1999) in axial flow, with a specific focus on the effects of localized non-uniformity. Furthermore, Chen and Hlavacek (Chen and Hlavacek, 1994) as well as Rogers and Long (Rogers and Long, 1997) utilized Voronoi tessellation to arrange fibers, which were generated through a random sequential addition, within the circular section of the shell. These latter two papers addressed the issue of fluid maldistribution within the fiber bundle only in axial flow.

Few researchers have investigated the effects of bundle non-uniformity in cross flow conditions. Among these, Howells (Howells, 1974) introduced a method for deriving averaged equations describing laminar flow within random arrays of aligned cylinders, both under axial and cross flow conditions. This approach utilized Brinkman's model, which explicitly considers the flow around a single fiber, treating the effects of all other nearby fibers as a Darcy resistance. Howells accounted for alterations in the mean flow, particularly in the near field, arising from the localized resistance characteristics. Consequently, he addressed the influence of a second fiber and averaged these effects across all its potential positions. The other authors who investigated cross flow conditions in random fiber distributions are Sangani and Yao (Sangani and Yao, 1988). They developed a numerical technique designed to compute the Darcy permeability in random arrangements of straight fibers, applicable to both axial and cross flow scenarios. This method was employed to investigate various configurations of periodic media, each composed of unit cells accommodating an increasing number of random fibers, ranging from 4 to 16. However, both these works have focused only on fluid dynamics, without delving into the issue of mass / heat transfer.

A complete review of the subject is beyond the scope of the present paper. In **Table 1**, the studies mentioned above have been organized and classified according to the specific topics and issues being investigated.

Despite this extensive literature, to the best of the authors' knowledge, a comprehensive description of the effects of non-uniform porosity on fluid dynamics and mass transfer within fiber bundles in the context of cross flow is still missing. Besides its intrinsic scientific interest, the problem finds practical applications, e.g. in the field of liquid-liquid or gas-liquid extraction in hollow fiber membrane contactors (Cai et al., 2016; Li and Zhang, 2018; Schöner et al., 1998; Zheng et al., 2005), where the increase of the shell-side mass transfer coefficient and the lower shell side pressure drop with respect to the parallel flow modules (Jansen et al., 1994; Wickramasinghe et al., 1992) provided by cross flow may enhance the module's performance.

This work represents an intermediate step in a research project started some years ago. The present authors have investigated the fluid dynamics and mass transfer in bundles of fibers arranged in regular lattices (Cancilla et al., 2021) and the effects of varying bundle porosity (Cancilla et al., 2023b). They have also explored the influence of non-uniform fiber distribution in axial flow (Cancilla et al., 2023a), considering simplified geometries made up by a checkerboard array of alternately high porosity and low porosity regions, each provided with a regular square lattice of fibers. The outcomes revealed that non-uniformity results in a significant increase in Darcy permeability and in a more pronounced reduction in the mass transfer coefficient. In the present study, we focus on exploring the effects of non-uniform distribution, but within the context of purely transverse flow, employing the same geometries previously scrutinized. Hence, the current investigation aims at pointing and understanding the implications of this non-uniformity by simulating a few rather extreme scenarios, without the additional complexities introduced by random distributions. Future research endeavors will be directed towards simulating configurations involving fibers randomly distributed across the plane.

Table 1: Literature works on the modelling of fiber bundles, divided according to the different issues investigated.

Authors and Ref.	Fiber arrangement	Non-uniformity	Axial flow	Cross flow	Mass transfer
(Miyagi, 1958)	square	☒	☒	☑	☒
(Happel, 1959)	square	☒	☑	☑	☒
(Sparrow and Loeffler, 1959)	square, hexagonal	☒	☑	☒	☒
(Dwyer and Berry, 1970)	hexagonal	☒	☑	☒	☑
(Howells, 1974)	random	☑	☑	☑	☒
(Noda and Gryte, 1979)	hexagonal	☒	☑	☒	☑
(Ishimi et al., 1987)	square, hexagonal	☒	☑	☒	☑
(Sangani and Yao, 1988)	random	☑	☑	☑	☒
(Miyatake and Iwashita, 1991, 1990)	hexagonal	☒	☑	☒	☑
(Chen and Hlavacek, 1994)	random	☑	☑	☒	☒
(Rogers and Long, 1997)	random	☑	☑	☒	☑
(Bao et al., 1999)	random	☑	☑	☒	☑
(Dierickx et al., 2001)	square, hexagonal	☒	☒	☑	☑
(Bao and Lipscomb, 2002a, 2002b)	random	☑	☑	☒	☑
(Cancilla et al., 2021)	square, hexagonal	☒	☑	☑	☑
(Sun et al., 2022)	square	☑	☑	☒	☑
(Cancilla et al., 2023a)	square	☑	☑	☒	☑

Regrettably, there is a conspicuous absence of experimental data in the existing literature for configurations closely resembling the one under investigation, rendering the task of validating our predictions unfeasible. Nevertheless, it is worth noting that numerical solutions for low Reynolds number steady laminar flow, achieved with meticulously refined grids and accurate numerical methods, can be considered virtually exact, often surpassing the precision attainable through experimental measurements.

2. Models and methods

2.1 Modelling assumptions

Numerical simulations were performed using the commercial finite volume code ANSYS CFX-18® (ANSYS, 2018). The modeling of the fiber bundle was guided by a set of simplifying assumptions:

1. The flow is perpendicular to the fibers, laminar, fully developed and steady.
2. The fibers are cylindrical, straight and parallel to the longitudinal z axis.
3. All fibers are identical in diameter.
4. All flow and concentration structures strictly adhere to the spatial periodicity of the fiber lattice.
5. The physical properties of the fluid (density, dynamic viscosity and scalar diffusivity) are constant.

The assumptions numbered from (1) to (4) facilitated the execution of simulations using the unit cell approach. Under this methodology, the computational domain comprised a recurrent and periodic unit of the bundle, encompassing a defined number of fibers (see Section 2.4).

2.2 Governing equations

The steady-state continuity and momentum equations for a Newtonian incompressible fluid can be written as:

$$\vec{\nabla} \cdot \vec{u} = 0 \tag{1}$$

$$\rho \vec{u} \cdot \vec{\nabla} \vec{u} = -\vec{\nabla} p + \mu \nabla^2 \vec{u} + \vec{F} \tag{2}$$

where $\vec{u}$ is the velocity vector, p is the pressure and $\vec{F}$ is a body force per unit volume acting along the flow direction, i.e. the driving pressure gradient compensating the large-scale pressure loss; ρ and μ are the density and the dynamic viscosity of the fluid.

The convection-diffusion transport equation assumed as the governing equation of the scalar field is given by:

$$\vec{u} \cdot \vec{\nabla} C = D \nabla^2 C + S_C \tag{3}$$

in which C is the scalar solute concentration and D is the diffusion coefficient of the solute in the fluid. The large-scale scalar gradient is compensated by the sink/source term S_C, derived by a global balance of solute in the computational domain. A more detailed explanation of the periodic unit cell approach is given in (Cancilla et al., 2021).

2.3 *Physical properties and boundary conditions*

The fluid properties were set equal to those of water at 25°C, so that the density ρ=997 kg/m^3 and the dynamic viscosity μ=8.89·10^{-4} Pa·s (Green and Perry, 2008). The study was conducted for a Schmidt number Sc=$\mu/(\rho \cdot D)$ of 500, representative of mass transfer of many species in water (e.g., urea and NaCl (Klein et al., 1976; Vitagliano and Lyons, 1956)). The choice of a high Schmidt number causes mass transfer phenomena (i.e., the behavior of the Sherwood number) to depend sensitively on the details of the flow field, advective fluxes being generally dominant with respect to diffusive ones even at relatively low Reynolds numbers (of the order of 1 or less). Therefore, many of the results regarding mass transfer obtained in the present work are specific of high-Sc conditions and would not be observed at Schmidt numbers of the order of 1 (this includes heat transfer with ordinary fluids such as water and gases, having a Prandtl number of ~1).

The variables simulated by the unit cell approach are the velocity $\vec{u}$ and the periodic component of the pressure p and of the scalar concentration C, so that periodic boundary conditions can be imposed to them between opposite boundaries of the computational domain.

In regard to hydrodynamics, a no slip condition was imposed at the cylindrical walls of the fibers. In regard to mass transfer, a Neumann boundary condition was adopted: the scalar flux from the wall into the fluid was set to an arbitrary uniform value of 10^{-5} mol·m^{-2}·s^{-1} (results are not affected by this value). This selection, as opposed to the Dirichlet boundary condition of imposed scalar concentration at the wall, aligns more closely with the actual operating conditions within a hollow fiber bundle. In the majority of applications related to membrane separation processes, such as hemodialysis, the resistance attributed to the membrane significantly outweighs that of the lumen and shell sides. Furthermore, this resistance is uniformly distributed circumferentially around each fiber. As a result, a near-uniform wall mass flux is expected.

2.4 *Computational domains and main definitions*

Two artificially designed cross-sectional geometries were simulated. The two computational domains, along with the definition of some relevant geometric quantities, are reported in **Figure 2**.

They comprise alternating square sections with varying porosities, organized in a checkerboard pattern. Within each section, the fibers were arranged in a square lattice. To account for symmetry, it was only necessary to include two low-porosity (“dense”) and two high-porosity (“loose”) square sections within the computational domain while enforcing lateral periodicity on the opposite sides. The same geometries were used by the authors to study the influence of the bundle non-uniform distribution on shell-side hydrodynamics and mass transfer for the case of purely axial flow (Cancilla et al., 2023a). The small and the large geometries share the same mean porosity ε. The former geometry comprises $N_d=2n_d^2=18$ fibers in the “dense” region and $N_l=2n_l^2=8$ fibers in the “loose” region, where n_d and n_l represent the number of fibers along each row or column of the respective square sub-region (the subscript d stays for “dense” and l for “loose”, respectively). Multiplying n_l, n_d by the same integer number (i.e., 2), a second geometry with 104 fibers was obtained. It was used to investigate the influence of the spatial scale of the non-uniformity.

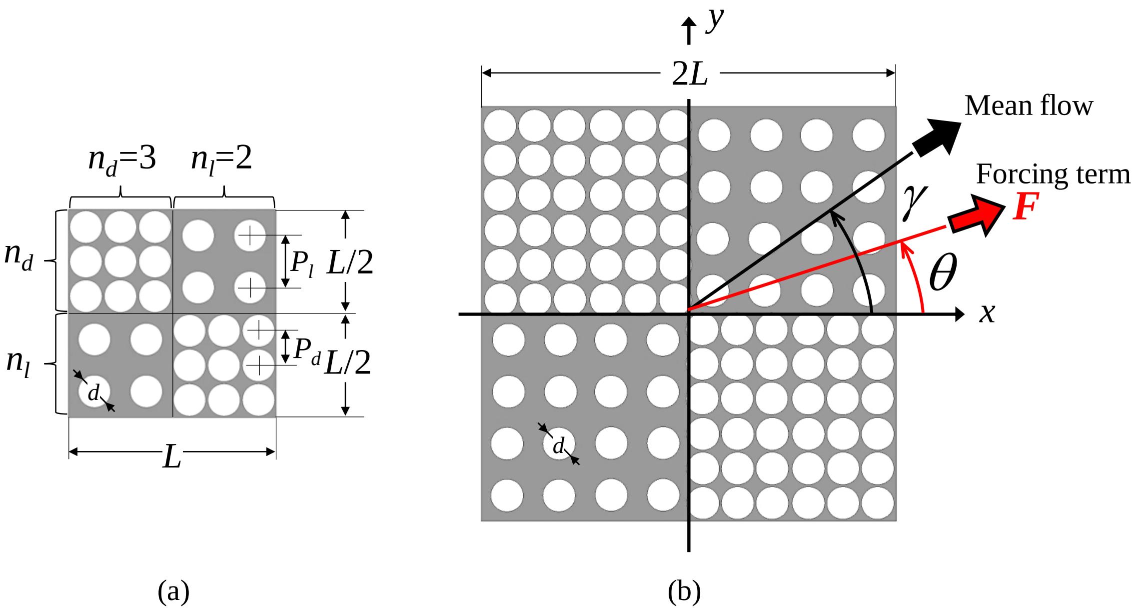

Figure 2: Cross section of the computational domains representing a fiber bundle divided into “dense” and “loose” regions arranged in a checkerboard pattern. (a) “small” geometry with 2×2 and 3×3= 26 fibers; (b) “large” geometry with 4×4 and 6×6= 104 fibers. n_d and n_l are the numbers of fibers along each row or column of the respective square sub-region.

P_l and P_d are the pitches of the “loose” and “dense” regions, defined as the center-center distances between adjacent fibers. The side lengths of the “small” and “large” computational domains are L and $2L$, respectively, whereas the dimension along the axial z direction was irrelevant and was arbitrarily established at 500 μm. The outer diameter of the fibers d was set to 280 μm, a typical value of commercial hemodialysis units. The mean porosity ε is defined here as:

$$\varepsilon = \frac{V}{V_{tot}} \tag{4}$$

where V is the fluid volume and the total volume V_{tot} is obtained by adding the volume of the fibers to V.

For each geometry in **Figure 2**, both the areas of the “dense” and “loose” square sub-regions and the diameters of the fibers are identical. Thus, the mean porosity can be expressed as the average of ε_l and ε_d:

$$\frac{\varepsilon_l + \varepsilon_d}{2} = \varepsilon \tag{5}$$

In the present work, the mean porosity was set to ε=0.5, while ε_l=0.69 and ε_d=0.31. For a comprehensive understanding of all the complete equations that connect the parameters ε, d, ε_l, ε_d, n_l, n_d, P_l, P_d and L, please consult Reference (Cancilla et al., 2023a).

According to **Figure 2**, one can define the cross flow attack angle, θ, as the angle between the forcing term $\vec{F}$ and the x axis, and the mean flow angle, γ, as the angle between the mean flow and the x axis. Note that $\gamma=\theta$ only in a hydraulically isotropic medium.

Consider $\langle \vec{u} \rangle$ as the *superficial* velocity vector, defined as the average of the local velocity $\vec{u}$ on the whole computational domain. It is also equal to the product of the mean porosity ε by the average of $\vec{u}$ over the fluid volume only (*interstitial* velocity). Throughout this paper, we will exclusively employ the *superficial* velocity, without reference to the *interstitial* velocity.

In the case of purely cross flow, forcing terms acting in various directions within the xy cross-sectional plane of the bundle are applied. The transverse flow Reynolds number Re_T was calculated as:

$$\mathrm{Re}_T = \frac{\rho \langle u_T \rangle d}{\mu} \tag{6}$$

using the mean *superficial* velocity u_T projected onto the direction of the applied forcing term:

$$\langle u_T \rangle = \langle u_x \rangle \cos\theta + \langle u_y \rangle \operatorname{sen}\theta \tag{7}$$

in which $\langle u_x \rangle$ and $\langle u_y \rangle$ denote the mean *superficial* velocities components along the x and y directions, respectively.

The Darcy-Weisbach friction coefficient f_T along the generic direction (T) within the cross-sectional plane is here defined as:

$$f_T = \frac{\left| \mathrm{d}p \,/\, \mathrm{d}T \right| \cdot 2d}{\rho \left\langle u_T \right\rangle^2} \tag{8}$$

Note that, based on the above definitions (6)-(8), one has:

$$f_T \cdot \mathrm{Re}_T = \frac{2}{K_T / d^2} \tag{9}$$

where $K_T=\mu\left\langle u_T \right\rangle/|\mathrm{d}p/\mathrm{d}T|$ is the cross flow hydraulic (Darcy) permeability of the bundle when subjected to a forcing term directed along T.

In regard to mass transfer, the average mass transfer coefficient is defined as:

$$U = \frac{\overline{J}}{\overline{C}_w - C_b} \tag{10}$$

in which $\overline{J}$ represents the wall-averaged molar flux at the wall, $\bar{C}_w$ is the wall-averaged molar scalar concentration at the wall and C_b is the bulk molar concentration, computed as the mass flow-weighted average of the scalar concentration on an arbitrary line cutting through the whole computational domain.

Consistently, the average Sherwood number Sh is calculated as:

$$\mathrm{Sh} = U \frac{d}{D} \tag{11}$$

In this work, the dimensionless quantities Re_T, f_T and Sh are defined on the basis of the outer fiber diameter d. An effective alternative is to define these quantities on the basis of the hydraulic diameter D_h= $4V/S$, in which S is the wet surface in the computational domain. However, for every lattice, the following relationship between D_h, d and ε is valid:

$$\frac{D_h}{d} = \frac{\varepsilon}{1-\varepsilon} \tag{12}$$

and given that, in the present study, the mean porosity is held constant at ε=0.5, according to Eq. (12) the definitions for Re_T, f_T and Sh based on d and D_h coincide.

2.5 *Domains discretization and numerical details*

The computational domain underwent discretization employing hybrid grids consisting of hexahedral and prismatic volumes. The adoption of hybrid meshes was imperative due to the intricate nature of the geometries under consideration, which proved challenging to mesh solely consisting of hexahedra. Nevertheless, it is worth noting that the utilized grids predominantly consist of hexahedral volumes, as detailed in **Table 2**.

Table 2: Summary of the grids employed.

Geometry	Number of finite volumes	% of volume discretized with hexahedra
small	~780,000	99.6
large	~3,120,000	99.7

In Reference (Cancilla et al., 2021) grids comprising approximately 10,000 volumes per fiber in the *xy* plane yielded results for the friction and mass transfer coefficients that exhibited a deviation of less than 1% compared to those obtained with the finest grid tested, which consisted of approximately 128,000 volumes per fiber in the *xy* plane. Consistently, a value of ~10,000 finite volumes per fiber was chosen as appropriate for the grids employed for all simulations in the present work. Details of the grids used are shown in **Figure 3**.

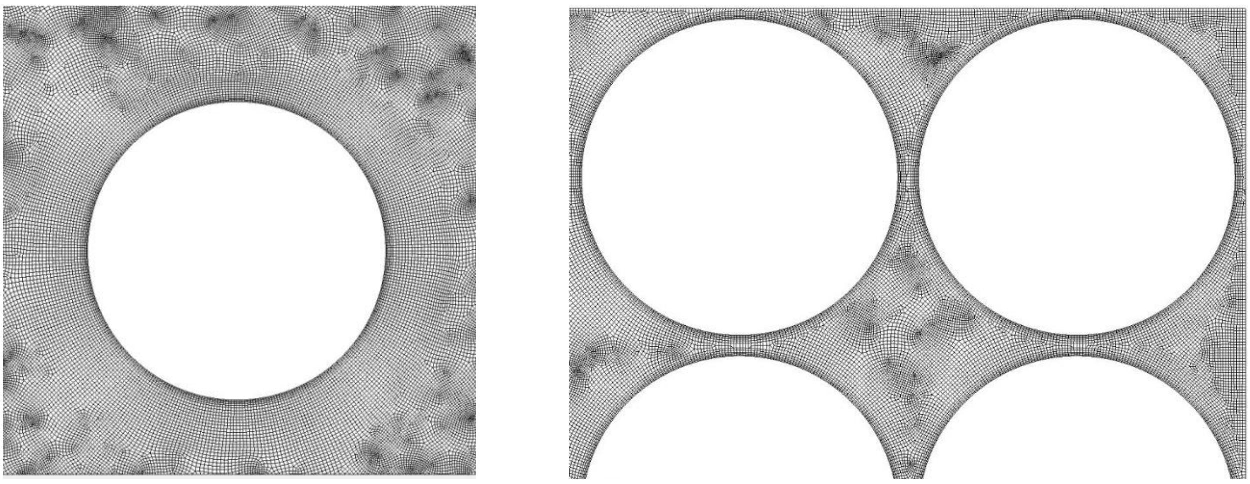

(a) (b)

Figure 3: Details of the mesh in the "loose" (a) and in the "dense" (b) regions. Each fiber is surrounded by an inflation layer that progressively refines the grid near the wall, to ensure a better resolution at the wall.

In the context of the current study, which focuses on investigating the impact of non-uniform porosity on friction and mass transfer coefficients within the fully developed region, the employed geometries were primarily two-dimensional. Therefore, the extent of the computational domains along the longitudinal direction held no significance. To align with the ANSYS-CFX code requirements, this extent was arbitrarily established at 500 μm and discretized using three finite volumes.

All simulations were conducted with a double-precision approach and were stopped when the dimensionless residuals of all variables decreased below 10^{-12}. Advection terms were discretized by a two-point upwind scheme. To solve for pressure and velocity, a strongly coupled algorithm was employed. In this study, the number of iterations, in the form of pseudo-time steps, varied based on the flow rate and the system geometry.

3. Results

A substantial volume of simulations was carried out, involving variations in the transverse flow Reynolds number (Re_T) and the flow attack angle (θ). It is important to note, as established in the existing literature (Williamson, 1996), that when Re_T exceeds 50, vortex shedding phenomena originate within the fluid, leading to the breakdown of the assumption of steady-state flow. To circumvent the complexities associated with time-dependent solutions, the present study exclusively examined cases with Re_T values ranging from 10^{-5} to 50. It is worth noting that within the computational domains under scrutiny, which consists of alternating square sections featuring varying porosities arranged in a checkerboard pattern with fibers positioned in a square lattice, the angular dependency of any parameter exhibits periodicity with a 90° period. However, it is sufficient to explicitly investigate flow attack angles within the range of 0° to 45° because the segment from 45° to 90° can be derived through symmetric reflection around the θ=45° axis.

Within each set of input data, the primary performance parameters reported were the product between the Darcy friction coefficient and the Reynolds number ($f_T{\cdot}\mathrm{Re}_T$) and the average Sherwood number (Sh).

3.1 Hydrodynamics

Figure 4(a, c) presents, in a semi-logarithmic scale, the product $f_T{\cdot}\mathrm{Re}_T$ as a function of Re_T for various values of θ, for the small and the large geometry, respectively. In the small geometry, graph (a), until a Reynolds number of approximately $\mathrm{Re}_T{\approx}1$ is reached, the Darcy friction coefficient (f_T) is independent on the flow attack angle (θ) and exhibits an almost exact inverse dependence with Re_T. This observation demonstrates that, at sufficiently low transverse Reynolds numbers (creeping flow), the fiber bundle under investigation behaves as a hydraulically isotropic medium, and the flow maintains a self-similar nature. At higher Reynolds numbers, when inertial forces become increasingly substantial, the behaviour of f_T deviates from the $(\mathrm{Re}_T)^{-1}$ trend and begins to exhibit a dependence on the flow attack angle θ. In the large geometry, graph (c), the friction coefficient behaves as $1/\mathrm{Re}_T$ up to $\mathrm{Re}_T \approx 1$, but even at very low Re values ($\mathrm{Re}_T \rightarrow 0$) it depends on the flow attack angle θ (hydraulic anisotropy).

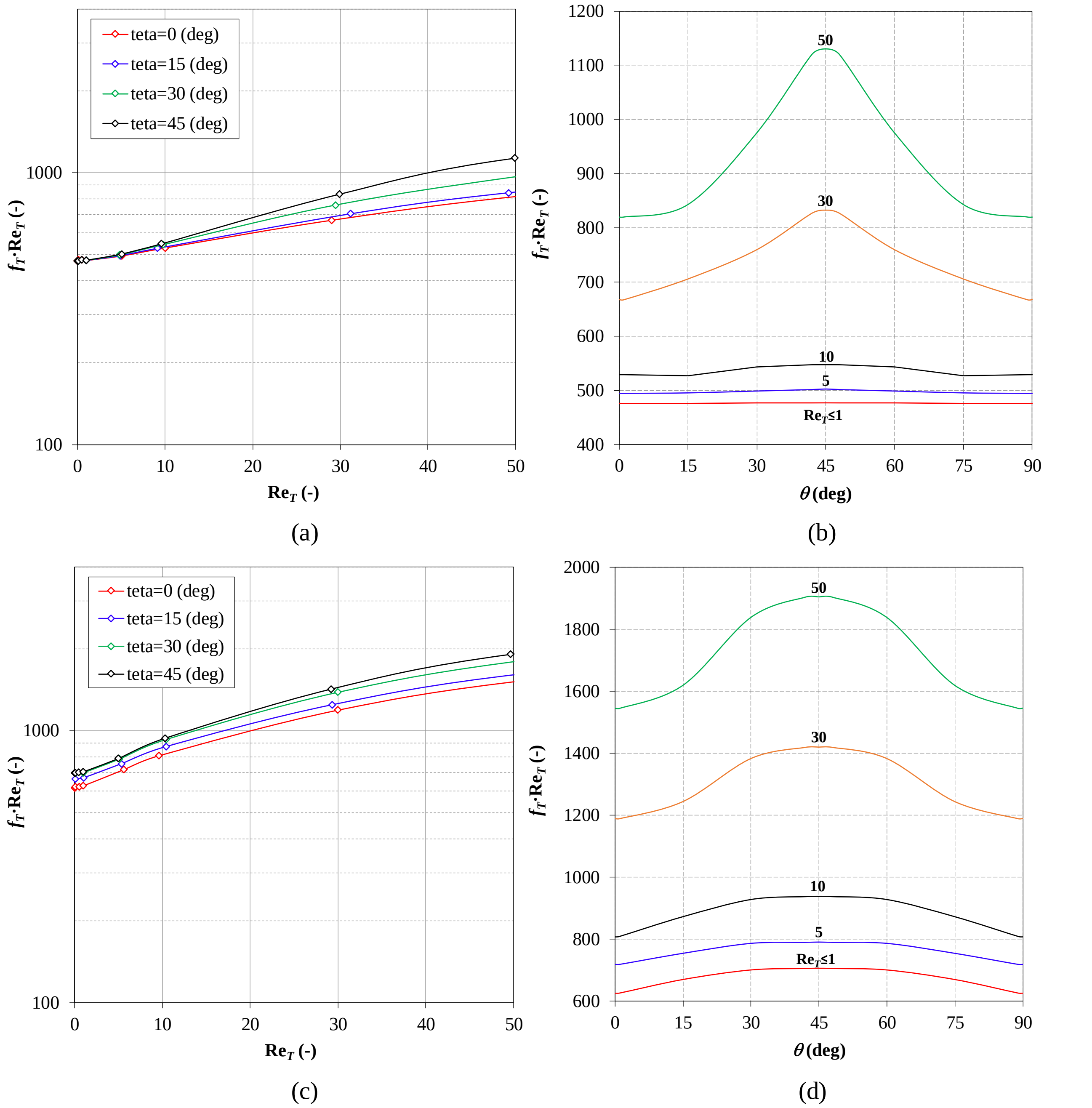

Figure 4: Product $f_T \cdot \mathrm{Re}_T$ (a, b) for the “small” geometry with 2×2 and 3×3 fibers and (c, d) for the “large” geometry with 4×4 and 6×6 fibers. (a, c) Semi-logarithm charts of $f_T \cdot \mathrm{Re}_T$ as a function of the transverse flow Reynolds number Re_T at different flow attack angles θ; (b, d) Product $f_T \cdot \mathrm{Re}_T$ as a function of θ (in the periodic range 0-90°) at different values of Re_T.

It is noteworthy that at θ=45°, the friction coefficient at Re_T=50 highly exceeds (~2.4 times for the small and ~2.7 times for the large geometry) the value predicted at low Reynolds numbers

($\mathrm{Re}_T \rightarrow 0$).

The relationship between the friction coefficient and the flow attack angle is more prominently displayed in **Figure 4**(b, d), which presents the product $f_T{\cdot}\mathrm{Re}_T$ as a function of θ for various values of the transverse flow Reynolds number, Re_T.

For the small geometry, graph (b), in accordance with the earlier observations, up to $\mathrm{Re}_T \approx 1$, θ exerts a minimal influence (indicating that the lattice behaves nearly as a hydraulically isotropic medium). However, as Re_T increases, $f_T{\cdot}\mathrm{Re}_T$ exhibits a minimum at θ=0°-90°, while reaching a maximum at 45°. This is not true for the large geometry in graph (d): in this case, even at $\mathrm{Re}_T << 1$, $f_T{\cdot}\mathrm{Re}_T$ exhibits a dependence on θ. The peaking factor, i.e. the ratio of angular maximum to angular average, is ~1.21 for the small geometry, and ~1.12 for the large one at Re_T=50.

In order to highlight the influence of non-uniformity on the friction coefficient, **Figure 5** reports in a double logarithmic scale the product $f_T{\cdot}\mathrm{Re}_T$ as a function of Re_T, for the small and the large geometries, in comparison with a regular square fiber arrangement at the same mean porosity ε=0.5. For the sake of brevity, just the cases for θ=0° (graph a) and 45° (graph b) are reported, but comparable plots and similar considerations also apply for the other angles investigated. In graph (c) the angular averaged values among all flow attack angles are reported.

For θ=0° (graph a), the lowest value for the friction coefficient is reached with the small geometry: the curve $f_T{\cdot}\mathrm{Re}_T$ is always below that for a regular square bundle, in the whole range of Re_T investigated. The minimum “small”-to-regular f_T ratio is ~0.75 and is attained for $\mathrm{Re}_T \rightarrow 0$, while it approaches 1 at Re_T=50. The behaviour of the large geometry is notably more intricate. The friction coefficient remains constant and ~5% below the curve for the regular square arrangement at the lowest Re_T (≤1). Subsequently, it begins to rise, and when Re_T exceeds 2, a reversal in hierarchy with respect to the regular square curve occurs.

For θ=45° (graph b), up to Re_T=1 the presence of a non-uniform porosity in the small domain reduces f_T by ~25% as in the case θ=0°, consequently leading to an equivalent enhancement in the flow rate for any given applied pressure difference. For Re_T =10, the variation in f_T is as low as ~17%. Unlike the case at θ=0°, the reversal in behaviour occurs for $\mathrm{Re}_T \approx 20$ and, at Re_T=50, f_T is ~44% larger compared to the regular square lattice curve. The curve for the large geometry exhibits a notable distinction from the previous one, remaining above that for the regular square lattice at all values of Re_T. For $\mathrm{Re}_T \leq 1$, the difference is ~8%, but it becomes much more pronounced as Re_T increases and is ~144% at Re_T=50.

The angular averaged behaviour (graph c) is very similar to those already discussed and similar considerations also apply. The crossing between the regular square and the small geometry curves occurs at $\mathrm{Re}_T \approx 30$, and the reversal in hierarchy takes place at Re_T >~40. On the other hand, the curve for the large geometry remains above that for the regular square lattice at all Re_T values.

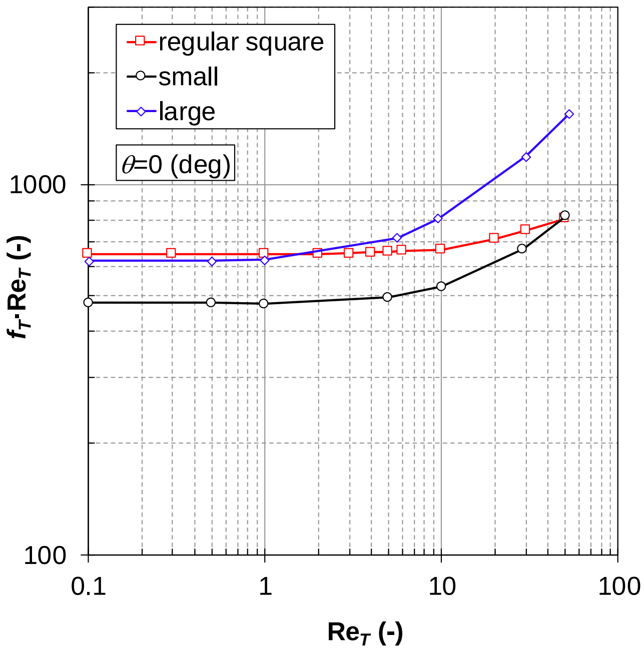

(a)

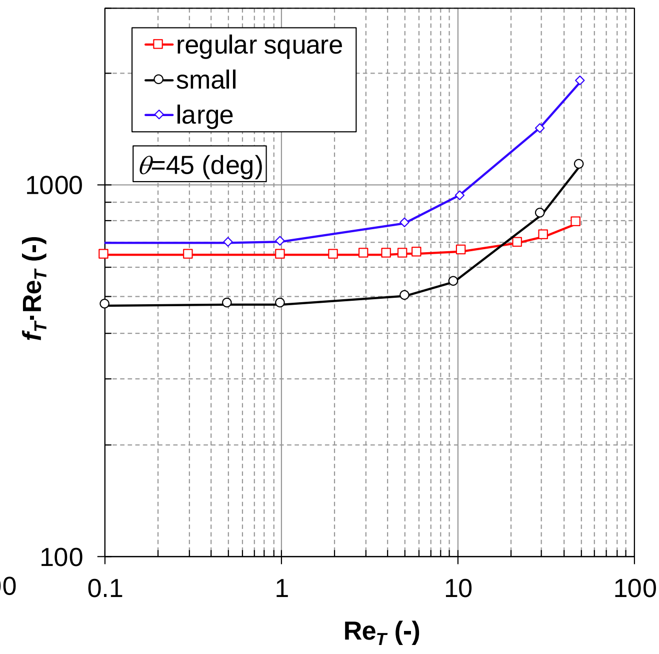

(b)

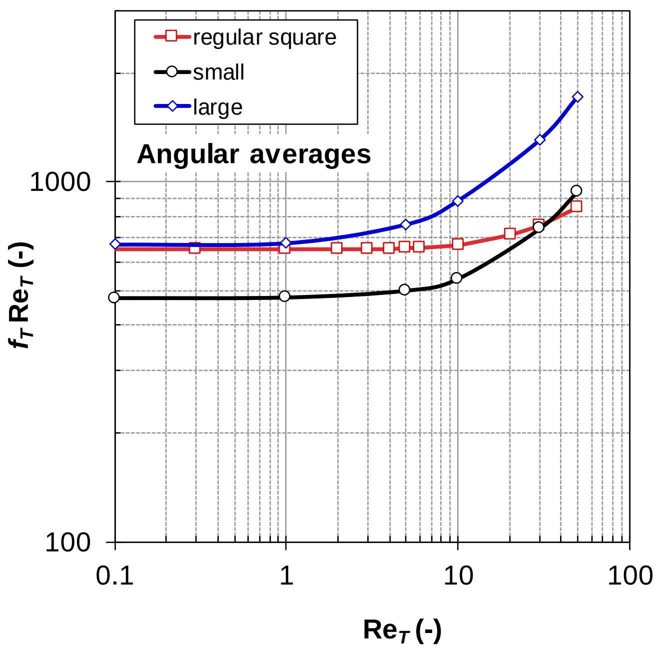

(c)

Figure 5: Double logarithmic chart of the product $f_T \cdot Re_T$ as a function of the transverse flow Reynolds number Re_T at θ=0° (a), θ=45° (b) and for the angular average (c). The graphs compare, for a porosity ε=0.5, the regular square lattice (squares) with the non-uniform "small" (circles) and "large" (diamonds) geometries.

It can be concluded that the effect of a non-uniform porosity on the friction coefficient in cross flow is rather complex. It depends on the cross flow attack angle, the Reynolds number (Re_T), and the scale of the non-uniformity considered. For Re_T<1, the product $f_T \cdot Re_T$ remains constant. However, for higher values of Re_T (particularly for Re_T>10), it increases more rapidly in geometries that exhibit a non-uniform porosity compared to the case of a regular lattice. As the angle θ varies, the qualitative trend remains the same, but the quantitative details change. This behavior is at strong variance with that observed for axial flow in the same non-uniform geometries, in which a non-uniform porosity always leads to a strong reduction of the friction coefficient (Cancilla et al., 2023a).

Simplified velocity maps and superimposed vector plots predicted at Re_T=1 in the small geometry when the forcing term $\vec{F}$ follows different directions are depicted in **Figure 6**.

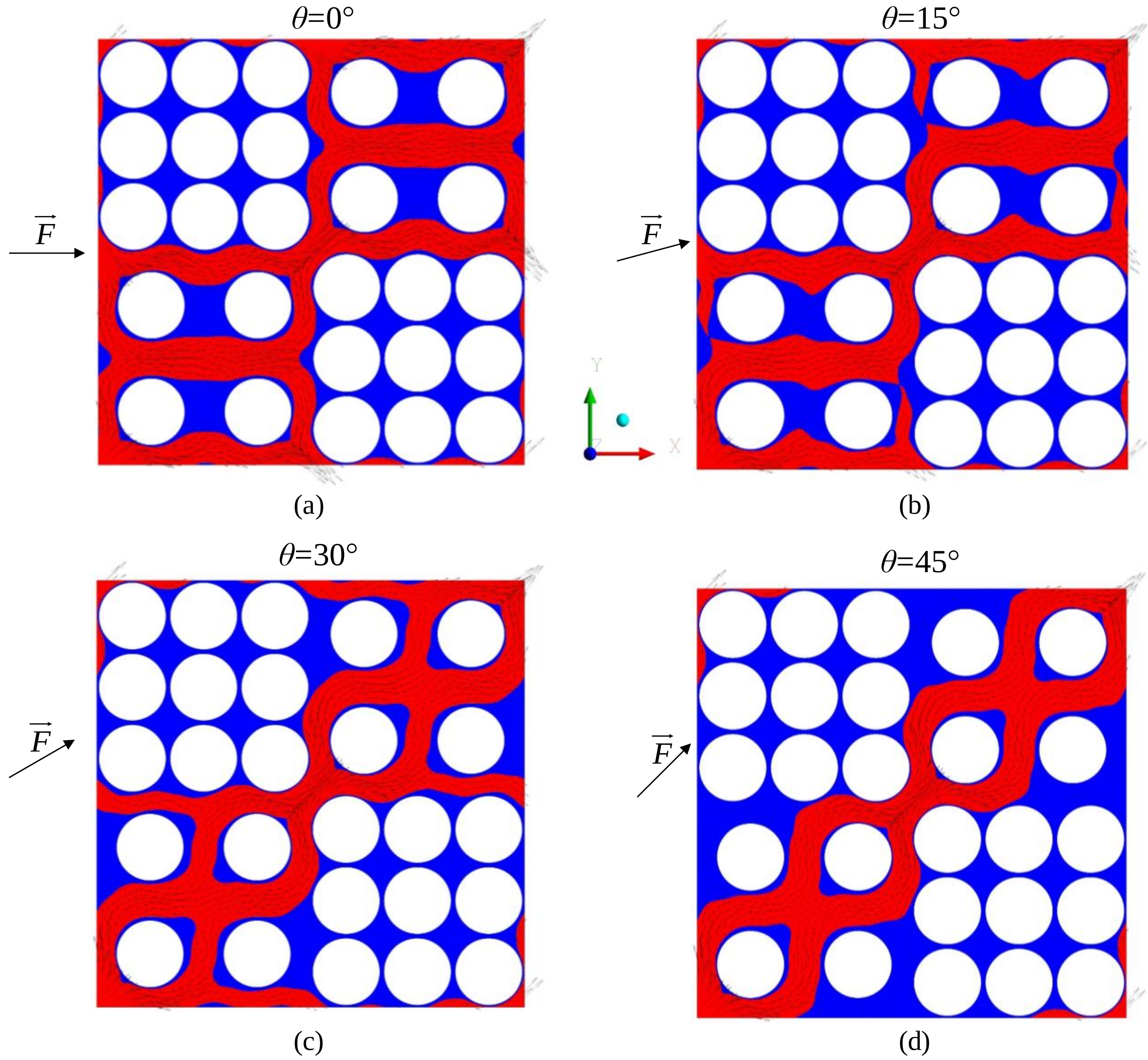

Figure 6: Simplified velocity maps and superimposed vector plots at Re_T=1 predicted for the “small” geometry with 2×2 and 3×3 fibers when the forcing term $\vec{F}$ is oriented at different angles. The direction of the forcing term $\vec{F}$ is shown and the angle θ formed with the x axis is reported. Blue regions: velocity<average velocity; red regions: velocity>average velocity.

Regions in which the velocity is larger than the average velocity (=0.0064 m/s) are indicated in red, regions where the velocity is smaller than the average velocity in blue. This representation is more effective than a continuous contour plot in order to show the flow topology.

The average velocity remains the same as the direction of $\vec{F}$ varies, confirming the hydraulic isotropy at Re_T=1. The fluid settles within the dense regions of the bundle, while it flows within the loose regions where peak values of several centimeters per second are reached. For all the simulated cross-flow attack angles, it appears that the dense regions are bypassed by the fluid, which perceives them as a single obstacle. However, the detachment and subsequent reattachment of the wake downstream of the fibers in the loose regions vary with changes in the forcing term direction. In particular, going from θ=0° to 45°, the fluid appears to shift from treating a pair of fibers as a single obstacle (maps a and b) to a complete detachment and reattachment on a fiber-by-fiber basis (maps c and d).

Figure 7 reports maps of the velocity module, normalized with respect to its (interstitial) average, along with superimposed vectors in the small geometry for θ=45°, and four different values of the transverse flow Reynolds number. The maps show that, as Re_T increases, the flow distributes itself increasingly among collateral channels between fibers, i.e., the relative importance of collateral pathways increases.

A noteworthy feature of the flow patterns in **Figure 6** and **7** is that in all cases the fluid flows mainly along preferential passages, mainly involving the “loose” regions, while some regions of the computational domain, including most of the “dense” regions, are essentially stagnant. This phenomenon, known in the literature as channeling, is typical of flow across fiber bundles, as already observed by various authors (Bao and Lipscomb, 2002a, 2002b; Li et al., 2016; Osuga et al., 2004; Ronco et al., 1997; Sun et al., 2022) and is expected to occur also in randomly distributed fiber bundles.

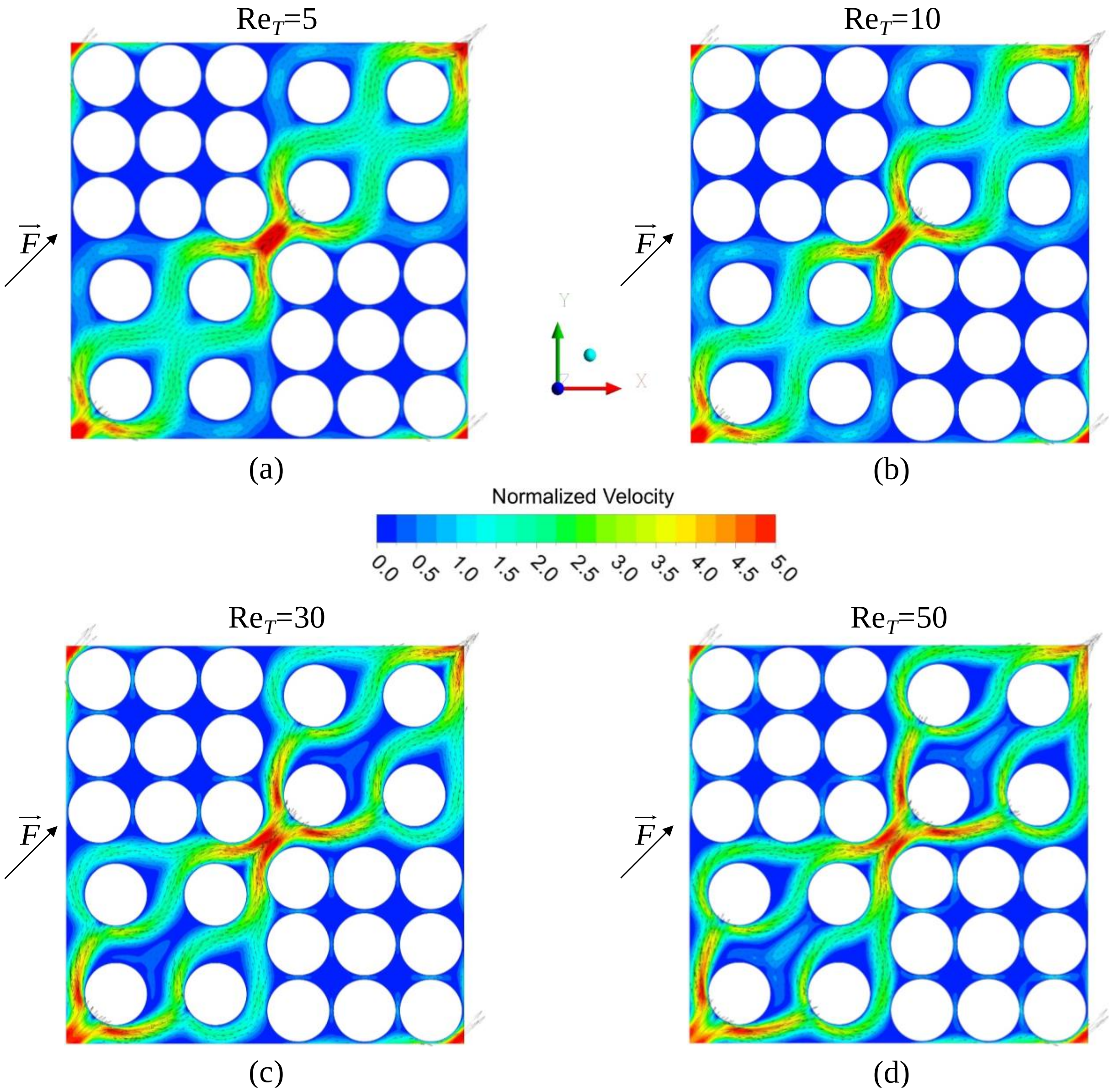

Figure 7: False color maps of the velocity module normalized with respect to its (interstitial) average and superimposed vector plots at θ=45° predicted for the "small" geometry with 2×2 and 3×3 fibers when the transverse flow Reynolds number Re_T ranges between 5 and 50. The direction of the forcing term $\vec{F}$ is shown and the value of Re_T is reported.

3.2 Mass transfer

In both the small and the large geometries, the Sherwood number (Sh) remains relatively uniform at all flow attack angles (θ) until a transverse Reynolds number of approximately 0.1 is attained. This observation suggests that at very low Reynolds numbers, the fiber bundle being studied demonstrates an isotropic behaviour, not only with regard to hydrodynamics, but also with regard to mass transfer. As the Reynolds number increases, Sh starts to show a correlation with the flow attack angle θ. Opposite to what was found for hydrodynamics, in regard to mass transfer the large geometry appears to be slightly less anisotropic with respect to the small geometry.

This behaviour is illustrated in **Figure 8**, which depicts the simultaneous dependence of mass transfer on the transverse flow Reynolds number and the cross flow attack angle.

Graphs (a) and (c) illustrate the behavior of Sh as a function of θ for several Re_T values ($1\cdot10^{-5}$, 0.001, 0.01, 0.1, 1, 10, 30, and 50). For clarity, the entire periodic range θ=0°-90° is displayed, although the profiles of all quantities exhibit symmetry with respect to θ=45° so that the interval 0-45° contains all the relevant information.

In the case of the small geometry (graph a), one can observe that:

- for $Re_T<10^{-4}$, the Sh vs. θ curves collapse into the same asymptotic profile;
- at all values of Re_T, the Sherwood number profile versus θ presents relative minima both at θ=45° and at θ=0°-90° and maxima at $\theta\approx$20°-30° and, symmetrically, 60°-70°;
- the degree of anisotropy with respect to mass transfer, expressed as $(Sh_{max}-Sh_{min})/Sh_{avg}$, is ~0.38 for $Re_T\rightarrow0$, increases up to a maximum of ~1.05 for $Re_T\approx1$, and then decreases for larger Re_T.

In the case of the large geometry (graph c), the picture is more complex:

- for $Re_T<10^{-4}$, the Sh vs. θ curves collapse into a single asymptotic profile as in the "small" geometry;
- this asymptotic profile for $Re_T\rightarrow0$ exhibits an absolute maximum for θ=45° and a shallow relative maximum for θ=0°-90° (not visible in **Figure 8**c);
- at values of Re_T between ~10^{-3} and ~30, the Sherwood number exhibits multiple maxima located at θ=45° and at $\theta\approx$15°-75° and multiple minima located at $\theta\approx$30°-60° and 0°-90°;
- at the largest Re_T investigated (50), the secondary minima at $\theta\approx$30°-60° and 0°-90° disappear while the maximum at θ=45° turns to a minimum, so that the Sherwood number exhibits only two minima at $\theta\approx$45° and 0°-90° and two maxima at $\theta\approx$20°-70°;
- the degree of anisotropy with respect to mass transfer, expressed as $(Sh_{max}-Sh_{min})/Sh_{avg}$, is more uniform than in the small geometry, exhibiting values of ~0.3-0.5 in the range Re_T=0.01 - 10, while it decreases both for Re_T below 0.01 and for Re_T above 10; it is ~0.09 for $Re_T\rightarrow0$, and ~0.18 for Re_T=50.

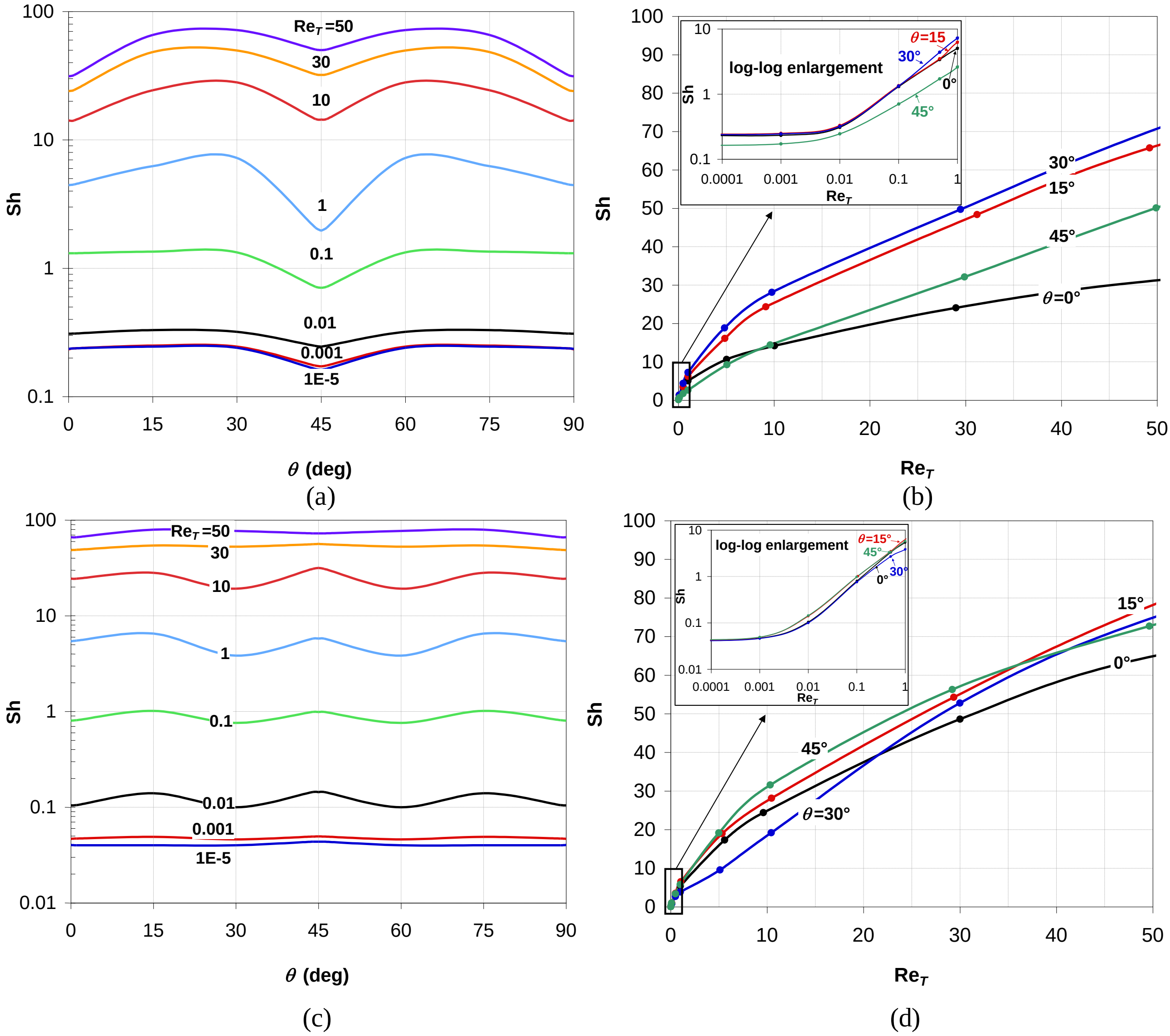

Figure 8: Sherwood number Sh (a, b) for the "small" geometry with 2×2 and 3×3 fibers and (c, d) for the "large" geometry with 4×4 and 6×6 fibers. (a, c) Sh as a function of θ (in the periodic range 0-90°) at different value of Re_T; (b, d) Sh as a function of the transverse flow Reynolds number Re_T at different flow attack angles θ. The insets show a double logarithmic enlargement in the range $10^{-4}<Re_T<1$.

Graphs b) and d) report Sh as a function of Re_T for four different values of θ (0°, 15°, 30° and 45°), for the small and the large domains, respectively.

In the small geometry (graph b), both for θ=0° (symmetry direction) and for intermediate flow attack angles, such as 15° and 30°, Sh increases ~twice as Re_T increases from 10 to 50; the increment is larger, from ~14 at Re_T=10 to ~50 at Re_T=50 (i.e., ~3.5-fold), for the case of θ=45° (second symmetry direction). The inset in Figure 7b reports (in a log-log scale) the behaviour of Sh at very low Re_T (from 10^{-4} to 1); it shows that, at all flow attack angles θ, Sh tends to an asymptotic value as $Re_T \rightarrow 0$, but a difference in Sh between different values of θ persists, confirming the existence of an asymptotic anisotropy in mass transfer.

In the large geometry (graph d), the anisotropy in Sh is less marked; the Sh curves for all angles θ remain closer to one another in the range Re_T=10 to 50. The Sherwood number increases from 20-30 at Re_T=10 to ~64-78 at Re_T=50 (i.e., from 2.3 to 3.7 times, much as in the small geometry). As the inset for low Re_T shows, also in this case Sh tends to asymptotic values for $Re_T \rightarrow 0$, but now the asymptotic angular distribution of Sh is more isotropic than in the small geometry (but not completely isotropic), as it is also shown by **Figure 8**c.

In order to highlight the effect of non-uniformity on mass transfer, **Figure 9** shows in double logarithmic charts the Sherwood number as a function of Re_T, for the small and the large geometries, in comparison with a regular square fiber array at the same mean porosity ε=0.5. For the sake of brevity, just the cases for θ=0° (graph a) and 45° (graph b) are reported, but equivalent plots and analogous considerations also apply for the others cross flow angles studied. In graph (c) the angular averaged values among all flow attack angles are reported.

For θ=0° (graph a), with both the non-uniform geometries under study, Sherwood numbers (Sh) remain constant up to $Re_T \approx 0.001$, exhibit a transitional behaviour in the range $0.001 < Re_T < 0.01$, and subsequently increase following a power law with slope ~1/2 for the small geometry and ~4/5 for the large geometry.

On the contrary, the regular square lattice exhibits a much flatter dependence on Re_T, with only a small increase of Sh form very low Re_T up to $Re_T \approx 10$.

Up to Re_T=0.1, the Sherwood number exhibits its lowest value in the large geometry. Conversely, the Sherwood number obtained with the small geometry falls between the previously mentioned value and the corresponding value computed for a regular square array under the same flow conditions. For Re_T<~1, non-uniform porosity has a detrimental impact on mass transfer. In the case of the small geometry, as $Re_T \rightarrow 0$ the Sherwood number decreases by ~16 times compared to that of a regular square array, while for the large geometry, Sh is reduced by a staggering 100 times (Sh≈4 in the regular bundle, Sh≈0.04 in the large geometry). These findings align with those previously discussed by the authors (Cancilla et al., 2023a) concerning purely axial flow. In that scenario, the transition from a regular square arrangement to the small and large domains resulted in a reduction of the fully developed values of Sh by a factor of ~25 (small geometry) and 100 times (large geometry), respectively.

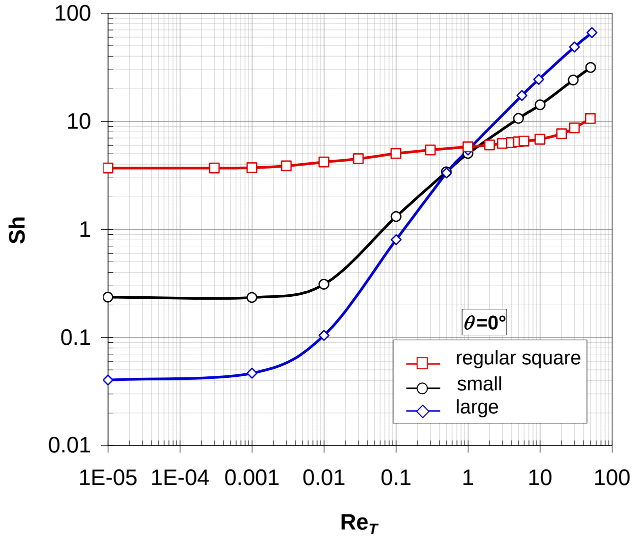

(a)

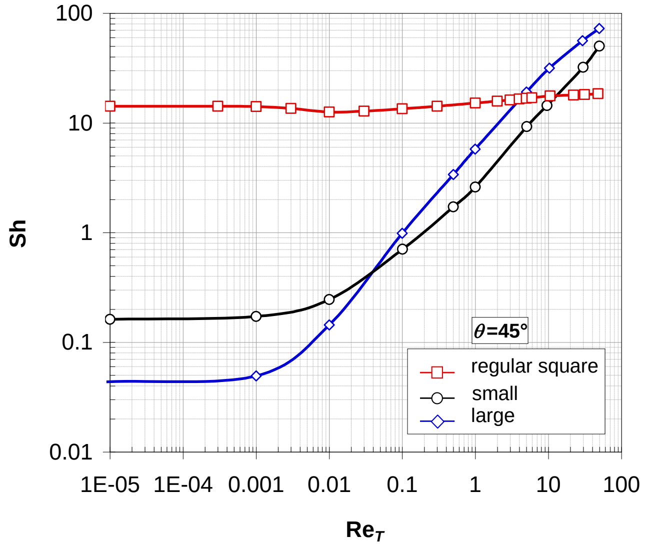

(b)

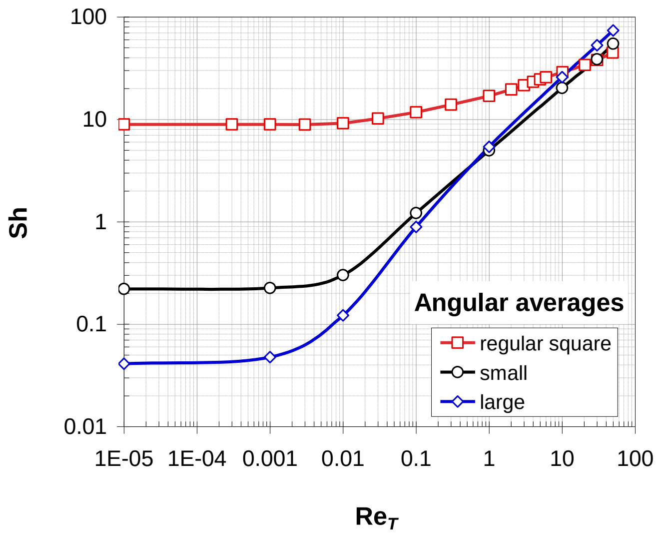

(c)

Figure 9: Sherwood number Sh as a function of the transverse flow Reynolds number Re_T in transverse flow at θ=0° (a), θ=45° (b) and for the angular average (c). The graph shows, for porosity ε=0.5, the comparison among the regular square lattice (squares) and the non-uniform "small" (circles) and "large" (diamonds) geometries.

For Re_T>0.1 the behaviour of Sh is more complex. The curves intersect each other within the range of Re_T values between 0.1 and 1, and when Re_T is larger than ~3, the hierarchy is completely reversed, the lowest Sh value being predicted for the regular square case and the highest one for the large geometry. Consequently, at high Reynolds numbers, the influence of a non-uniform porosity on mass transfer proves advantageous, leading to the potential achievement of a Sh enhancement by 3 to 6.5 times compared to that of a regular square bundle (Re_T=50).

For θ=45° (graph b), the curves of the Sherwood number exhibit a qualitatively similar behaviour. In the case of the small geometry, Sh begins to rise at Re_T=0.01, showing a power-low relationship of slope ~3/4 in the range $1<Re_T<50$. With the large geometry, the value of Sh for $Re_T \to 0$ is lower but the rate of increase is similar, with a slope of about 3/4 in the range $0.1<Re_T<10$. Contrariwise, the regular array geometry exhibits a much flatter Re_T-dependence of Sh, and even a slight decrease in the range $10^{-3}<Re_T<10^{-2}$. As $Re_T \to 0$, a non-uniform porosity has an even more significant effect on mass transfer for θ=45° than for θ=0°. In the small geometry, the Sherwood number experiences a reduction of approximately 80-fold in comparison to its regular array value (Sh≈14). In the case of the large geometry, Sh undergoes an even larger reduction, decreasing by ~325-fold (Sh≈0.043) when compared to that of a regular square array. Unlike the case at θ=0°, the intersection of the Sh curves occurs at an earlier point, specifically at $Re_T \approx 0.1$. However, the reversal in hierarchy occurs later, at Re_T values exceeding approximately 20, and when Re_T=50 simulations indicate a notable enhancement in Sh, ~2.7 (small geometry) to ~4 (large geometry) times larger than that of a regular square bundle.

The angular averaged behaviour (graph c) is very similar to those already discussed and similar considerations also apply. With the small geometry, the Sherwood number starts to increase at Re_T=0.01, exhibiting a power-law relationship with a slope of ~3/5. The large geometry shows a lower Sh value for $Re_T \to 0$, but the rate of increase is larger, with a slope of about 0.7 in the range $0.1<Re_T<50$. The regular array geometry shows a much shallower Re_T-dependence of Sh, even indicating a slight increase with a slope of ~0.23 in the range $1<Re_T<30$.

The crossing of the Sh profiles occurs at $Re_T \approx 1$, and the reversal in hierarchy takes place at Re_T values larger than ~40. When Re_T=50, simulations indicate an increase in Sh of approximately 1.2 times larger for the small geometry and approximately 1.6 times larger for the large geometry compared to a regular square bundle. Consequently, when considering angle-averaged values of the Sherwood number, the enhancement is shifted toward higher Re_T values, and it appears to be softened.

Figure 10 shows maps of the dimensionless concentration in the large geometry for the transverse flow Reynolds number Re_T=1 and two values of the cross flow attack angle, i.e. 15° and 30°, corresponding to the highest (~6.5) and lowest (~3.8) Sherwood number (see **Figure 8**c).

The dimensionless concentration is defined here as:

$$C^* = \frac{C}{C_b} \tag{13}$$

where C_b is the mass flow-weighted average of the scalar concentration on an arbitrary cross section, i.e. the bulk concentration.

Note that in **Figure 10** the same scale is used for both maps. For either value of θ, the “dense” regions, where the fluid flows with lower velocities, are characterized by higher dimensionless concentrations and vice versa (i.e., little mixing). For θ=15° the map exhibits a flatter distribution of the dimensionless concentration, while for θ=30° it exhibits a broader range of C^* values.

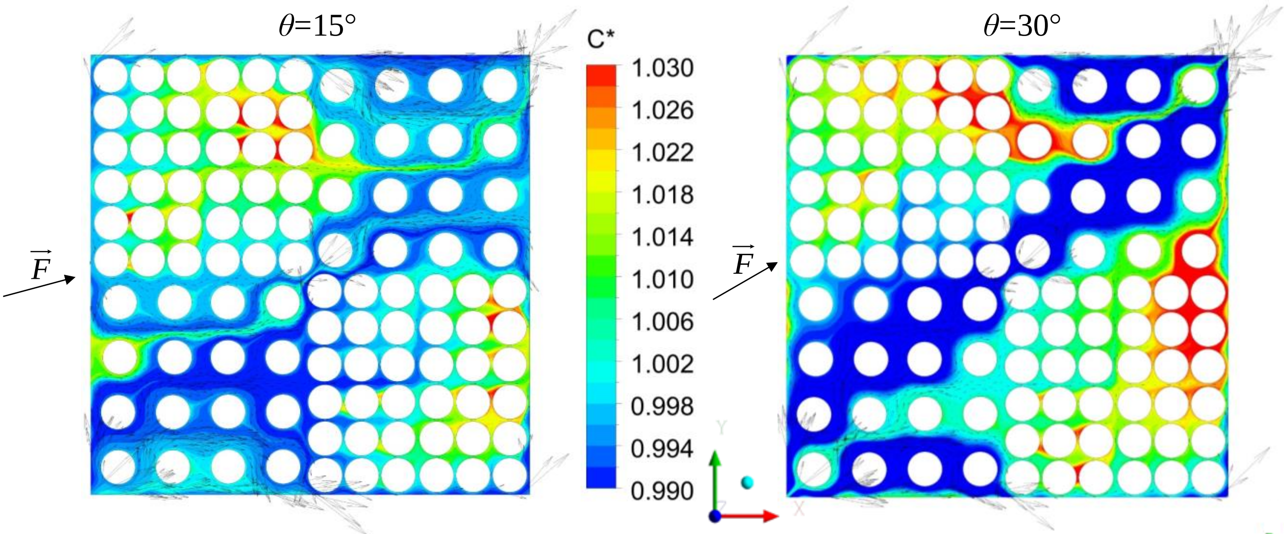

(a) (b)

Figure 10: False color maps of the dimensionless concentration and superimposed vector plots at Re_T=1 predicted for the "large" geometry with 4×4 and 6×6 fibers when the forcing term $\vec{F}$ is oriented at different angles. The direction of the forcing term $\vec{F}$ is shown and the angle θ formed with the x axis is reported.

Figure 11 provides insights into how the flow, even at such low Reynolds numbers, has a significant impact on the scalar distribution. It reports maps of the dimensionless concentration in the large geometry for a cross flow attack angle of 45° and three different values of the transverse flow Reynolds number ($1\cdot10^{-5}$, 0.001 and 0.01, respectively). Corresponding maps for the small geometry are qualitatively similar and are not shown for the sake of brevity.

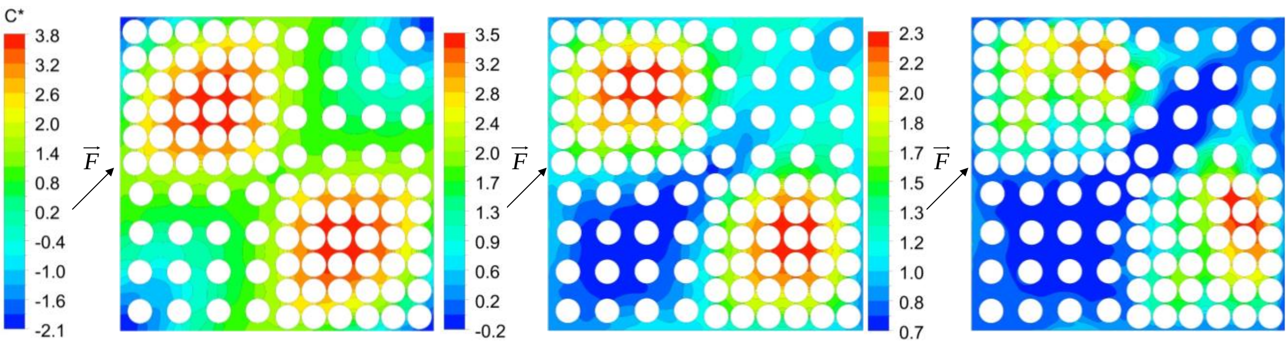

(a) (b) (c)

Figure 11: Dimensionless concentration predicted for the "large" geometry with 4×4 and 6×6 fibers for θ=45° and three values of the transverse flow Reynolds number: (a) $Re_T=1\cdot10^{-5}$; (b) Re_T=0.001; (c) Re_T=0.01.

At Re_T=1·10^{-5} (map a), the distribution is nearly symmetrical between the upstream and downstream the dense and the loose regions. However, at Re_T=0.001 and 0.01, which are still hydrodynamically creeping flows (maps b and c), the effects of advection break this symmetry, resulting in a noticeably asymmetric scalar distribution. This behaviour can be attributed to the high Schmidt number (500): the transverse Péclet number, Re_T·Sc, is 0.005 in case (a), while it is 0.5 in case (b) and 5 in case (c). These last two values, while small, are not negligible. Even at such low Re_T, the concentration distribution does not exhibit a centrally symmetric configuration as one would observe in pure diffusion or purely axial flow.

Figure 12 presents the Sherwood number as a function of the cross flow attack angles (θ) at various Re_T for both the regular square array and the small non-uniform geometry.

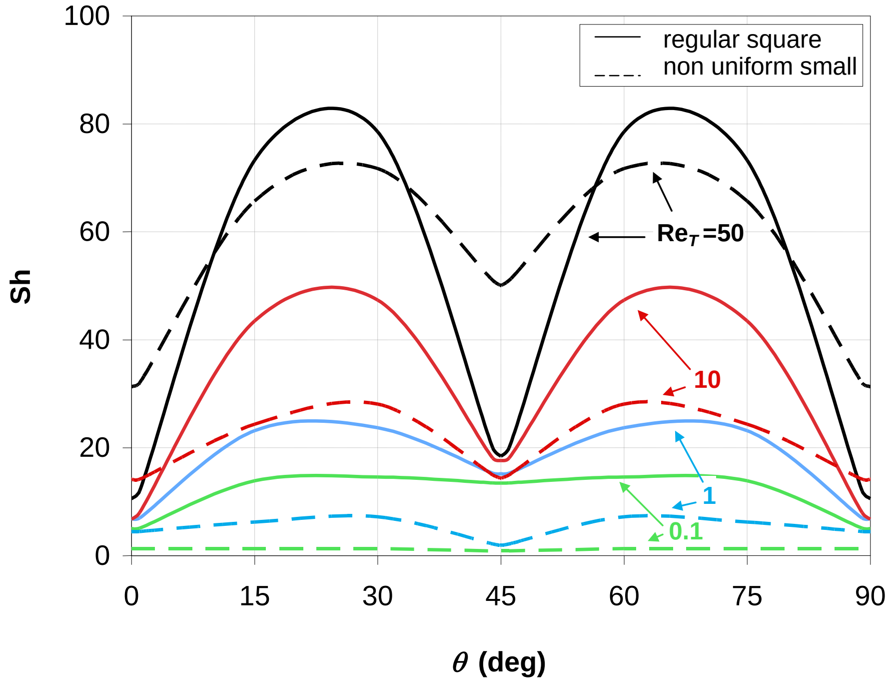

Figure 12: Sherwood number Sh as a function of the flow attack angles θ (in the periodic range 0-90°) at different value of the transverse flow Reynolds number Re_T. The graph shows, for porosity ε=0.5, the comparison among the regular square lattice (solid lines) and the "small" geometry with 2×2 and 3×3 fibers (broken lines).

The comparison reveals that up to Re_T=10 the dashed curves, which are the non-uniform small geometry, consistently exhibit lower values of the Sherwood number across all cross flow attack angles, in comparison with the solid curves which are for the regular square lattice. The sole exceptions to this trend occurs at Re_T=10 for θ=0°-90°, where $Sh_{non\text{-}unif}$≈14 while Sh_{unif}≈7, and at Re_T=50 both for θ=0°-5° or θ=85°-90° (symmetrically) and for θ=35°-55°. On average, the reduction in Sh is ~2-fold for Re_T=10 but increases at low Re_T and is as large as ~3 for Re_T=1 and

~10 for Re_T=0.1. However, the reduction in the Sherwood number is far smaller than that observed in axial flow (Cancilla et al., 2023a), where it can be as high as 25 (small geometry) and 100 (large geometry) at Re_T=10.

Thus, the presence of non-uniform porosity leads to a reduction in the Sherwood number and, consequently, a decrease in mass transfer compared to the scenario with a bundle of uniformly distributed fibers with regular porosity. Furthermore, when comparing the curves with the same Re_T (e.g., the green lines for Re_T=0.1), it is evident that the profiles in the case of non-uniform porosity are, on average, flatter than those in the case of uniform porosity. This implies that, in regard to mass transfer, non-uniformity tends to reduce the anisotropy compared to the situation with uniform porosity. This effect is even more pronounced when considering the large geometry as can be inferred by comparing graphs (a) and (c) in **Figure 8**.

The decrease in overall mass transfer coefficients due to the uneven distribution of porosity, which leads to the flow being diverted towards regions with higher porosity (commonly known as channeling), has also been experimentally verified by several researchers. For instance, Ronco and co-workers (Ronco et al., 1997) noted that the inclusion of spacing yarns between the fibers in hemodialyzers improved module performance by mitigating channeling. Additionally, irregularities in flow and concentration distribution in hemodialyzers resulting from non-uniform porosity were explored using imaging techniques like proton magnetic resonance (Osuga et al., 2004). The reduction in the efficiency of toxin removal due to uneven flow distribution was quantitatively characterized through the combined use of imaging techniques and computational fluid dynamics (Li et al., 2016). Recently, Sun *et al.* (Sun et al., 2022) predicted that channeling phenomena, arising from the bypass formed in the fluid flow pattern between the fiber bundle and the module housing, have a detrimental impact on module performance.

In summary, the impact of non-uniform porosity on mass transfer in cross flow is a rather intricate matter. It hinges on various factors, including the cross-flow attack angle, Reynolds number (Re_T), and the length scale of the non-uniformity in consideration. For Re_T<0.001, the Sherwood number remains constant and falls far below the values achieved in a regular fiber distribution. At higher Re_T values, Sh begins to increase, and upon reaching a critical Re_T threshold, its growth becomes more rapid in configurations that incorporate non-uniform porosity when contrasted with a lattice featuring uniform porosity. While the qualitative trend persists as the angle θ changes, the specific Re_T value at which the curves intersect varies.

Conclusions

This study focuses on non-uniform porosity within fiber bundles, particularly in cross-flow conditions, which is a less-explored area in the existing literature. The impact of non-uniform porosity on both hydrodynamics and mass transfer is examined at varying Reynolds numbers and flow attack angles.

The simulated model channel was conceptually divided into alternating "dense" and "loose" regions, arranged in a checkerboard pattern, with each region containing a regular array of fibers. Fully developed simulations were performed, assuming periodic boundary conditions between all opposing faces of the computational domain. Two distinct sizes for the "dense" and "loose" regions were taken into account: one involving 2×2 and 3×3 fibers (referred to as the small geometry), and the other consisting of 4×4 and 6×6 fibers (designated as the large geometry). These configurations are, of course, highly artificial, but reflect some aspects of the local irregularities actually occurring in large real bundles of randomly packed fibers while allowing, thanks to their well defined geometry, a quantitative non-statistical assessment of the influence of non-uniformity.

In regard to hydrodynamics, a non-uniform porosity had a complex effect on the friction coefficient, influencing it differently in small and large geometries. Overall, non-uniform porosity led to a reduction in the Darcy friction coefficient (f_T), especially at lower Reynolds numbers. In the small geometry, the friction coefficient remained relatively uniform with the flow attack angle (θ) at low Reynolds numbers (Re_T<1), indicating hydraulic isotropy. At higher Reynolds numbers, f_T exhibited dependency on the flow attack angle. In contrast, the large geometry showed such dependency even at low Reynolds numbers ($\mathrm{Re}_T \rightarrow 1$). By comparison, regular fiber arrays in cross-flow exhibited hydraulic isotropy for all $\mathrm{Re}_T \leq \sim 1$.

In regard to mass transfer, a non-uniform porosity generally led to lower Sherwood numbers (Sh) compared to regular square arrays, especially at low Reynolds numbers. However, at high Reynolds numbers, non-uniform porosity could enhance mass transfer in certain scenarios. In the small geometry, the Sherwood number remained almost uniform with respect to the flow attack angle θ at very low Reynolds numbers, indicating mass transfer isotropy. As the Reynolds number increased, Sh correlated more and more with θ. The large geometry exhibited less anisotropy in mass transfer compared to the small geometry, a behaviour opposite to that observed for the friction coefficient.

These findings highlight the significance of non-uniform porosity in influencing fluid dynamics and mass transfer in cross-flow hollow fiber contactors, with implications for various applications, such as liquid-liquid or gas-liquid extraction.

Obtaining accurate measurements of local flow and, to an even greater extent, mass transfer in geometries resembling those under investigation would present significant challenges. Nevertheless, numerical solutions for flow and mass transfer under conditions of low Reynolds numbers (characterized by steady laminar flow) can be considered virtually exact when achieved with well-resolved grids and accurate numerical methods. In fact, these numerical solutions tend to be more accurate than any conceivable measurement. Furthermore, although there is a lack of experimental data for the specific conditions examined in this study, the overarching conclusions drawn here, such as the reduction of both friction and mass transfer coefficients in non-uniform bundles (at least for the case of purely axial flow) in comparison to uniform ones, have been validated by numerous studies in the existing literature. These studies encompass a range of approaches, including experimental, theoretical, and computational analyses, as exemplified by the works of Lipscomb and co-workers (Bao et al., 1999; Bao and Lipscomb, 2002a, 2002b).

This paper primarily focused on scalar transfer, considering it as mass transfer and characterizing it with Schmidt and Sherwood numbers. However, the same problem can be reinterpreted as a heat transfer process, with the associated numbers being Prandtl and Nusselt numbers. This expanded viewpoint allows the conclusions to be applicable to a broader range of applications, including mini-heat exchangers and various heat transfer devices.

Acknowledgments

Part of this work was carried out with the financial support of the *Programma Operativo Nazionale Ricerca e Innovazione 2014-2020 (CCI 2014IT16M2OP005), Fondo Sociale Europeo, Azione I.1 "Dottorati Innovativi con caratterizzazione Industriale"*.

Nomenclature

C	concentration (mol m^{-3})
C^*	dimensionless concentration (-)
D	scalar diffusivity (m^2 s^{-1})
d	outer diameter of a fiber (m)
D_h	hydraulic diameter (m)
$\vec{F}$	forcing term compensating the large-scale pressure gradient (Pa)
f	Darcy-Weisbach friction coefficient (-)
J	mass flux at the wall (mol m^{-2} s^{-1})
K	Darcy permeability (m^2)

L	length along x and y directions (m)
N	number of fibers (-)
n	number of fibers on each side (-)
P	pitch (center-center distance between adjacent fibers) (m)
p	pressure (Pa)
Pe	Péclet number, Re·Sc (-)
Re	Reynolds number (-)
S	wet surface of the computational domain (m^2)
S_C	source term compensating the large-scale concentration gradient (mol m^{-3} s^{-1})
Sc	Schmidt number (-)
Sh	Sherwood number (-)
T	cross flow direction (-)
U	local shell side mass transfer coefficient (m s^{-1})
$\vec{u}$	velocity vector (m s^{-1})
V	volume (m^3)
x, y	Cartesian coordinates in cross section orthogonal to the fibers (m)
z	Cartesian coordinate along the axial direction (m)

Greek symbols

γ	mean flow angle (deg)
ε	mean porosity (-)
θ	cross flow attack angle (deg)
μ	dynamic viscosity (Pa s)
ρ	density (kg m^{-3})

Subscripts

b	bulk (mass flow averaged)
d	"dense" (low porosity)
l	"loose" (high-porosity)
T	cross flow direction
tot	total
w	wall
x, y	coordinates

Averages

$\bar{\cdot}$ surface average

$\langle\cdot\rangle$ volume average

References

ANSYS, 2018. ANSYS CFX Reference Guide Release 18.2.

Bansal, B., Gill, W.N., 1982. Hollow Fiber Reverse Osmosis Systems Analysis and Design. Chem. Eng. Commun. 18, 311–330. https://doi.org/10.1080/00986448208939973

Bao, L., Lipscomb, G.G., 2002a. Well-developed mass transfer in axial flows through randomly packed fiber bundles with constant wall flux. Chem. Eng. Sci. 57, 125–132. https://doi.org/10.1016/S0009-2509(01)00368-2

Bao, L., Lipscomb, G.G., 2002b. Mass transfer in axial flows through randomly packed fiber bundles with constant wall concentration. J. Memb. Sci. 204, 207–220. https://doi.org/10.1016/S0376-7388(02)00043-1

Bao, L., Liu, B., Lipscomb, G.G., 1999. Entry mass transfer in axial flows through randomly packed fiber bundles. AIChE J. 45 (11), 2346–2356. https://doi.org/10.1016/S0927-5193(03)80004-9

Cai, J.J., Hawboldt, K., Abdi, M.A., 2016. Analysis of the effect of module design on gas absorption in cross flow hollow membrane contactors via computational fluid dynamics (CFD) analysis. J. Memb. Sci. 520, 415–24. https://doi.org/10.1016/j.memsci.2016.07.054

Cancilla, N., Gurreri, L., Ciofalo, M., Cipollina, A., Tamburini, A., Micale, G., 2023a. Hydrodynamics and mass transfer in straight fiber bundles with non-uniform porosity. Chem. Eng. Sci. 279, 118935. https://doi.org/10.1016/j.ces.2023.118935

Cancilla, N., Gurreri, L., La Rosa, M., Ciofalo, M., Cipollina, A., Tamburini, A., Micale, G., 2023b. Influence of bundle porosity on shell-side hydrodynamics and mass transfer in regular fiber arrays: A computational study. Int. J. Heat Mass Transf. 203, 123841. https://doi.org/https://doi.org/10.1016/j.ijheatmasstransfer.2022.123841

Cancilla, N., Gurreri, L., Marotta, G., Ciofalo, M., Cipollina, A., Tamburini, A., Micale, G., 2022. A porous media CFD model for the simulation of hemodialysis in hollow fiber membrane modules. J. Memb. Sci. 646, 120219. https://doi.org/10.1016/j.memsci.2021.120219

Cancilla, N., Gurreri, L., Marotta, G., Ciofalo, M., Cipollina, A., Tamburini, A., Micale, G., 2021. CFD prediction of shell-side flow and mass transfer in regular fiber arrays. Int. J. Heat Mass Transf. 168, 120855. https://doi.org/https://doi.org/10.1016/j.ijheatmasstransfer.2020.120855

Chen, V., Hlavacek, M., 1994. Application of Voronoi tessellation for modeling randomly packed hollow-fiber bundles. AIChE J. 40, 606–612. https://doi.org/10.1002/aic.690400405

Dierickx, P.W., De Wachter, D.S., Verdonck, P.R., 2001. Two-dimensional finite element model for oxygen transfer in cross-flow hollow fiber membrane artificial lungs. Int. J. Artif. Organs 24, 628–635. https://doi.org/10.1177/039139880102400904

Dwyer, O.E., Berry, H.C., 1970. Laminar-Flow Heat Transfer for in- Line Flow Through Unbaffled Rod Bundles. Nucl. Sci. Eng. 42, 81–88. https://doi.org/10.13182/nse70-a19330

Frank, A., Lipscomb, G.G., Dennis, M., 2000. Visualization of concentration fields in hemodialyzers by computed tomography. J. Memb. Sci. 175, 239–251.

https://doi.org/https://doi.org/10.1016/S0376-7388(00)00421-X

Green, D.W., Perry, R.H., 2008. Perry's Chemical Engineers' Handbook, 8th ed. McGraw-Hill, New York.

Happel, J., 1959. Viscous flow relative to arrays of cylinders. AIChE J. 5, 174–177. https://doi.org/10.1002/aic.690050211

Howells, I.D., 1974. Drag due to the motion of a Newtonian fluid through a sparse random array of small fixed rigid objects. J. Fluid Mech. 64, 449–476. https://doi.org/10.1017/S0022112074002503

Ibrahim, M.H., El-Naas, M.H., Zhang, Z., Van Der Bruggen, B., 2018. CO2 Capture Using Hollow Fiber Membranes: A Review of Membrane Wetting. Energy and Fuels 32, 963–978. https://doi.org/10.1021/acs.energyfuels.7b03493

Ishimi, K., Koroyasu, S., Hikita, H., 1987. Mass transfer in creeping flow past periodic arrays of cylinders. J. Chem. Eng. Japan 20(5), 492–498. https://doi.org/10.1252/jcej.20.492

Jansen, A.E., Klaassen, R., Feron, P.H.M., Hanemaaijer, J.H., ter Meulen, B.P., 1994. Membrane gas absorption processes in environmental applications, in: Crespo, J.G., Boddeker, K.W. (Eds.), Membrane Processes in Separation and Purification. Kluwer Academic, Dordrecht, pp. 343–356. https://doi.org/10.1007/978-94-015-8340-4_16

Klein, E., Holland, F., Lebeouf, A., Donnaud, A., Smith, J.K., 1976. Transport and mechanical properties of hemodialysis hollow fibers. J. Memb. Sci. 1, 371–396. https://doi.org/10.1016/S0376-7388(00)82283-8

Li, G.P., Zhang, L.Z., 2018. Three-dimensional turbulent flow and conjugate heat and mass transfer in a cross-flow hollow fiber membrane bundle for seawater desalination. Int. J. Heat Mass Transf. https://doi.org/10.1016/j.ijheatmasstransfer.2017.12.044

Li, W., Liu, Jing, He, L., Liu, Juanjuan, Sun, S., Huang, Z., Liang, X.M., Gao, D., Ding, W., 2016. Simulation and experimental study on the effect of channeling flows on the transport of toxins in hemodialyzers. J. Memb. Sci. 501, 123–133. https://doi.org/10.1016/j.memsci.2015.11.037

Miyagi, T., 1958. Viscous Flow at Low Reynolds Numbers past an Infinite Row of Equal Circular Cylinders. J. Phys. Soc. Japan. https://doi.org/10.1143/JPSJ.13.493

Miyatake, O., Iwashita, H., 1991. Laminar-flow heat transfer to a fluid flowing axially between cylinders with a uniform wall heat flux. Int. J. Heat Mass Transf. 34, 322–327.

Miyatake, O., Iwashita, H., 1990. Laminar-flow heat transfer to a fluid flowing axially between cylinders with a uniform surface temperature. Int. J. Heat Mass Transf. 33, 417–425. https://doi.org/10.1252/kakoronbunshu.13.152

Nakatsuka, S., Nakate, I., Miyano, T., 1996. Drinking water treatment by using ultrafiltration hollow fiber membranes. Desalination 106, 55–61. https://doi.org/10.1016/S0011-9164(96)00092-6

Noda, I., Brown-West, D.G., Gryte, C.C., 1979. Effect of flow maldistribution on hollow fiber dialysis - experimental studies. J. Memb. Sci. 5, 209–225. https://doi.org/10.1016/S0376-7388(00)80449-4

Noda, I., Gryte, C.C., 1979. Mass Transfer in Regular Arrays of Hollow Fibers in Countercurrent Dialysis. AIChE J. 25, 113–122. https://doi.org/https://doi.org/10.1002/aic.690250113

Osuga, T., Obata, T., Ikehira, H., 2004. Detection of small degree of nonuniformity in dialysate flow in hollow-fiber dialyzer using proton magnetic resonance imaging. Magn. Reson. Imaging 22, 417–420. https://doi.org/10.1016/j.mri.2003.08.008

Rogers, J.D., Long, R.L., 1997. Modeling hollow fiber membrane contactors using film theory, Voronoi tessellations, and facilitation factors for systems with interface reactions. J. Memb. Sci. 134, 1–17. https://doi.org/10.1016/S0376-7388(97)00074-4

Ronco, C., Scabardi, M., Goldoni, M., Brendolan, A., Crepaldi, C., La Greca, G., 1997. Impact of spacing filaments external to hollow fibers on dialysate flow distribution and dialyzer performance. Int. J. Artif. Organs 20, 261–266. https://doi.org/10.1177/039139889702000505

Sangani, A.S., Yao, C., 1988. Transport processes in random arrays of cylinders. II. Viscous flow. Phys. Fluids 31, 2435–2444. https://doi.org/10.1063/1.866596

Schöner, P., Plucinski, P., Nitsch, W., Daiminger, U., 1998. Mass transfer in the shell side of cross flow hollow fiber modules. Chem. Eng. Sci. 53, 2319–2326. https://doi.org/10.1016/S0009-2509(98)00097-9

Sparrow, E.M., Loeffler, A.L., 1959. Longitudinal laminar flow between cylinders arranged in regular array. AIChE J. 5, 325–330. https://doi.org/10.1002/aic.690050315

Sun, L., Panagakos, G., Lipscomb, G., 2022. Effect of Packing Nonuniformity at the Fiber Bundle–Case Interface on Performance of Hollow Fiber Membrane Gas Separation Modules. Membranes (Basel). 12, 1139. https://doi.org/10.3390/membranes12111139

Teber, O.O., Altinay, A.D., Mehrabani, S.A.N., Tasdemir, R.S., Zeytuncu, B., Genceli, E.A., Dulekgurgen, E., Pekkan, K., Koyuncu, İ., 2022. Polymeric hollow fiber membrane oxygenators as artificial lungs: A review. Biochem. Eng. J. 180. https://doi.org/10.1016/j.bej.2022.108340

Vitagliano, V., Lyons, P.A., 1956. Diffusion Coefficients for Aqueous Solutions of Sodium Chloride and Barium Chloride. J. Am. Chem. Soc. 78, 1549–1552. https://doi.org/10.1021/ja01589a011

Voronoi, G., 1908. Nouvelles applications des parametres continus a la theorie des forms quadratiques. J. Reine Angew. Math. 133, 97–178.

Wickramasinghe, S.R., Semmens, M.J., Cussler, E.L., 1992. Mass transfer in various hollow fiber geometries. J. Memb. Sci. 69, 235–250. https://doi.org/10.1016/0376-7388(92)80042-I

Williamson, C.H.K., 1996. Vortex dynamics in the cylinder wake. Annu. Rev. Fluid Mech. 28, 477–539. https://doi.org/10.1146/annurev.fl.28.010196.002401

Yang, X., Yu, H., Wang, R., Fane, A.G., 2012. Optimization of microstructured hollow fiber design for membrane distillation applications using CFD modeling. J. Memb. Sci. 421–422, 258–270. https://doi.org/10.1016/j.memsci.2012.07.022

Zheng, J.M., Dai, Z.W., Wong, F.S., Xu, Z.K., 2005. Shell side mass transfer in a transverse flow hollow fiber membrane contactor. J. Memb. Sci. 261, 114–120. https://doi.org/10.1016/j.memsci.2005.02.035